RESEARCH ARTICLE

small methods
www.small-methods.com

Unraveling the Atomistic Mechanisms Underlying Effective Reverse Osmosis Filtration by Graphene Oxide Membranes

Shan Jiang, Lingli Huang, Honglin Chen, Jiong Zhao, and Thuc Hue Ly**

The graphene oxide (GO) membrane displays promising potential in efficiently filtering ions from water. However, the precise mechanism behind its effectiveness remains elusive, particularly due to the lack of direct experimental evidence at the atomic scale. To shed light on this matter, state-of-the-art techniques are employed such as integrated differential phase contrast-scanning transmission electron microscopy and electron energy loss spectroscopy, combined with reverse osmosis (RO) filtration experiments using GO membranes. The atomic-scale observations after the RO experiments directly reveal the binding of various ions including Na^+, K^+, Ca^{2+}, and Fe^{3+} to the defects, edges, and functional groups of GO. The remarkable ion-sieving capabilities of GO membranes are confirmed, which can be attributed to a synergistic interplay of size exclusion, electrostatic interactions, cation–π, and other non-covalent interactions. Moreover, GO membranes modified by external pressure and cation also demonstrated further enhanced filtration performance for filtration. This study significantly contributes by uncovering the atomic-scale mechanism responsible for ion sieving in GO membranes. These findings not only enhance the fundamental understanding but also hold substantial potential for the advancement of GO membranes in reverse osmosis (RO) filtration.

1. Introduction

GO has attracted significant attention in recent years as a highly promising material for advanced filtration membranes due to its excellent filtration performances, including high throughput, fast transport rate, and outstanding chemical stability.[1] Indeed, the feasibility of water filtration utilizing GO membranes was initially demonstrated in the 1970s, wherein clay-encapsulated GO membranes were employed in RO filtration.[2] Nevertheless, the potential use of GO membranes for filtration is overshadowed by their relatively fragile instability, especially when compared to robust thin-film composite membranes,[3] which have been widely employed in the filtration industry for decades.[4] Recently, researchers have renewed their interest in GO materials, due to their increased global production and considerably lowered costs.[5] Following the groundbreaking discovery of monolayer graphene in 2004, GO has once again emerged as a promising member of 2D materials, attracting significant attention in academic research.[6]

GO is a chemically modified form of graphene/graphite, produced by the introduction of oxygen-containing functional groups onto the graphene lattice through oxidation processes.[7] Functional groups, such as hydroxyl (–OH), epoxy (–O–), and carboxyl (–COOH) groups, are introduced in GO and disrupt the sp^2 hybridization of carbon atoms. As a result, GO exhibits distinct electrical, mechanical, and chemical properties when compared to pristine graphene.[8] The oxygen functional groups on GO surfaces provide water solubility, enabling GO lamellar membrane formation via vacuum, evaporation, or pressure-assisted self-assembly techniques.[9] The proposed mechanism of GO

S. Jiang, L. Huang, T. H. Ly
City University of Hong Kong Shenzhen Research Institute
Shenzhen 518000, China
E-mail: thuchly@cityu.edu.hk

S. Jiang, L. Huang, T. H. Ly
Department of Chemistry and Center of Super-Diamond & Advanced Films
City University of Hong Kong
Kowloon, Hong Kong P. R. China

The ORCID identification number(s) for the author(s) of this article can be found under https://doi.org/10.1002/smtd.202400323

DOI: 10.1002/smtd.202400323

S. Jiang, H. Chen, J. Zhao
Department of Applied Physics
The Hong Kong Polytechnic University
Kowloon, Hong Kong China
E-mail: jiongzhao@polyu.edu.hk

S. Jiang, H. Chen, J. Zhao
The Hong Kong Polytechnic University Shenzhen Research Institute
Shenzhen 518000, China

T. H. Ly
Department of Chemistry and State Key Laboratory of Marine Pollution
City University of Hong Kong
Kowloon, Hong Kong 999077, P. R. China

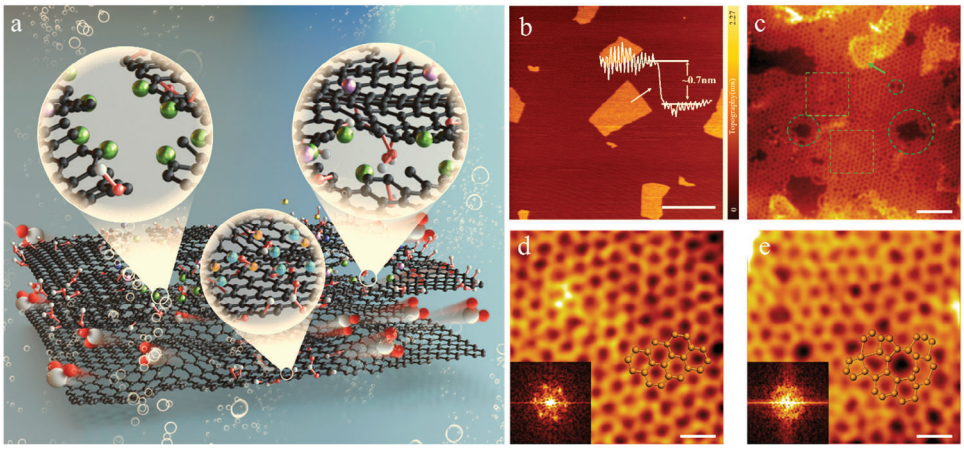

Figure 1. GO membrane for RO filtration. a) Schematic illustration of water transport and ion trapping in defects, edges, and functional groups in channels of GO membrane during RO filtration. b) AFM topography of monolayer GO sheets on f-mica substrate. Scale bar 500 nm. c) High-resolution iDPC-STEM image of monolayer GO with different types of defects. Scale bar 2 nm. d,e) Magnified iDPC-STEM images from marked box (lower and upper) areas in (c), respectively. The inset shows FFT images from the same area in (c). Scale bar 500 pm.

membrane responsible for salt exclusion primarily involves size sieving (interlayer filtration), Donnan exclusion (electrostatic repulsion), and the adsorption of ions onto GO nanosheets through cation–π interactions, π–π interactions, or other non-covalent interactions.[10]

Interlayer filtration is widely acknowledged as the predominant mechanism utilized by GO-based membranes for the selective separation of particles or molecules of varying sizes and shapes.[11] The interlayer spacing of GO membranes can be adjusted by controlling the stacking arrangement of GO layers and the density of functional groups, which selectively allows smaller substances to pass through while blocking larger ones. Interlayer sieving is also known to be dependent on the humidity of the surrounding environment. The water permeation capacity of stacked GO membranes used for nanofiltration may be notably constrained by their inherent propensity to undergo swelling, whereby water is absorbed into the GO channels, leading to an expansion of the interlayer spacing.[12] In recent years, GO-based composites have been widely used to overcome the swelling issue such as GO/MOF composite,[13] GO/metal oxide composite,[14] GO/polymer composite,[15] GO/cations composite,[16] and so on.

Currently, the filtering mechanism of the GO membrane is still a subject of debate, and there is a lack of direct experimental evidence.[17] While previous studies have primarily focused on interlayer sieving by tuning the interlayer spacing of GO membrane, our study here highlights the critical role played by the intralayer atomic defects (pores), edges, and functional groups of GO in water filtration. Especially when considering smaller ions present in seawater, the expansion of the interlayer spacing and damage in structure reduces the interlayer sieving capability and enhances the significance of basal plane defects for overall sieving performance. Moreover, during the RO process, the trapping of ions or ion clusters at these nanometer-scale basal-plane defects or edge defects in GO could obstruct the originally unimpeded or even barrier-free ion penetration pathway, thereby enhancing the filtration performances.

2. Results and Discussion

2.1. Preparation of GO Membrane for RO Experiment

The salt exclusion mechanisms in GO membrane involve various processes, such as interlayer sieving, coupled with water transport. In this process, water molecules gather in hydrophilic regions and then enter hydrophobic 2D nanochannels within the GO structure.[9] This allows water molecules to permeate while effectively blocking the dissolved solids, ions, and impurities, thus enabling efficient water transport and separation in filtration processes (**Figure 1**a). In our experiment, to create the GO membrane with sub-nanometer channels for RO filtration, the monolayer GO sheets are first prepared through the modified Hummers' method,[7,18] and then the dispersed monolayer GO sheets are stacked into continuous GO films (Figure S1, Supporting Information) through self-alignment under gravity by vacuum filtration, see Methods and Figure S2 (Supporting Information) for details.[19] Atomic force microscopy (AFM) topographic image (Figure 1b) reveals a thickness of ≈0.7 nm for the monolayer GO on fluorphlogopite mica (f-mica) substrate, while the macro-stacked GO membrane, consisting of numerous monolayers GO sheets, has a thickness of ≈100 nm (Figure S3, Supporting Information).

2.2. Atomic Structures of GO

The atomic structure of the membrane determines the filtration capability. To gain insights into the atomic structure changes of the GO membrane during the RO process, we use the mechanical exfoliation method to obtain monolayer and few-layer GO flakes directly from the GO membrane before and after the filtration processes, respectively. The GO flakes are then transferred onto a Quantifoil Au TEM grid (Figure S4, Supporting Information), and a weak Ar-only plasma treatment is applied to remove the hydrocarbon contaminants before TEM measurement. Raman spectra in Figure S5 (Supporting Information) show that transfer and Ar plasma treatment will not cause obvious changes to

the GO samples that were used for TEM measurement, which is specifically reflected in no changes in the intensity ratio of I_D/I_G (related defects) and I_{2D}/I_G (related to functional groups) in Table S1 (Supporting Information). Before this step, the residual salt solution on the surface of the wet membrane after the RO experiment has been removed. To reduce the knock-on beam damage and enhance the imaging contrast of light elements, the low dose Cs-corrected iDPC-STEM technique,[20] is applied to investigate the atomic structures of monolayer and few-layer GO sheets during TEM characterization. It is worth emphasizing that oxygen-containing functional groups cannot be directly obtained in high-resolution STEM images due to their ultra-beam-sensitive nature. For a typical atomic scale STEM image in our experiment, an electron dose of 5×105 e^- $Å^{-2}$ is applied for each image to ensure sufficient image contrast for such monoatomic-layer samples. At such electron density level, the oxygen atoms are easily removed during beam irradiation as evidenced by Figures S6 and S7 (Supporting Information).

The atomic structure of GO is heterogeneous and mainly composed of aromatic graphitic islands, constituted of unoxidized condensed benzene rings, and oxidized sp^3 carbon atom regions with aliphatic six-membered rings (Figure 1c). The chemical composition and size of these domains depend on the degree of oxidation. Beam-sensitive functional groups in GO are removed under beam irradiation,[21] which makes the percentage of O element ranging from 43.25% to 6.18% (Figure S8 and Table S2, Supporting Information), leaving a graphene-like structure in most of the regions of GO basal plane, and oxygen doping only can be observed in a few areas, as shown in Figure S9 (Supporting Information). For monolayer GO, the high-resolution iDPC-STEM image in Figure 1c displays highly inhomogeneous structures. As the degree of oxidation increases, the diffraction spots of hexagonal graphene significantly decrease (Figure 1d,e), and Fast Fourier Transform (FFT) analysis also reveals the intensity of amorphous rings increases in different regions from Figure 1c. Correspondingly, the intensity of diffraction spots associated with graphene structure diminishes gradually. The amorphous region exhibits a much broader variation, with in-plane projections of bond lengths ranging from 1.36 to 1.73 Å, and bond angles vary between 82° and 152° as shown in Figure S10 (Supporting Information). This stands in sharp contrast to graphene, where the bond lengths are centered at ≈1.4 Å and bond angles ≈120° with only small variations attributed to image aberration errors. Crystalline graphene is projected to reach its breaking point at deformations of just under 1.6 Å and 135°.[22] Consequently, amorphous GO is different from graphene and would be inherently stable.

Moreover, various-sized pore defects (marked by green circles in Figure 1c) which are released during the aggressive oxidation and sheet exfoliation, make the intralayer structure of GO sheets become intricate and variable. Furthermore, small GO nanosheets (marked by a green arrow) resulting from the fragmentation of other layers also make the structure of GO complicated. The Raman spectrum of pristine GO sheets in Figure S10 (Supporting Information) exhibits characteristic G bands (≈1588 cm^{-1}) originating from the planar vibrations of carbon atoms, along with D bands (≈1352 cm^{-1}) associated with structural defects.[23] Additionally, following beam irradiation, an enhancement in the intensity of the 2D peak can be associated with a reduction of oxygen-containing functional groups within the basal plane. Conversely, a shift towards lower wavenumbers (from 2688 to 2654 cm^{-1}) of the 2D peak is indicative of an increase in the degree of reduction.[24] The full width at half maximum (FWHM) of the 2D peak shows a climb from 84.35 cm^{-1} to 120.22 cm^{-1} which is due to new defects (Figure S13, Supporting Information) caused by the beam damage during irradiation. Typically, GO has a carbon/oxygen (C/O) ratio of 1.5–2.5 and can be produced by different chemical methods.[24b] However, in high-resolution STEM images, we can only find some doping oxygen elements with low density (0.04 ± 0.01 nm $^{-2}$) in the GO lattice (Figure S9, Supporting Information) in high-resolution STEM images. The EDS result shows there is ~6% oxygen left after beam irradiation. During TEM measurement, most of the O atoms turn into gaseous molecules and are removed from the TEM techniques, while the other O atoms combine with C atoms and become amorphous and indistinguishable.

In general, although we try to reduce the beam effect during STEM measurement, it is important to note that GO undergoes an inevitable reduction process, resulting in the loss of its original oxygen-containing functional groups. Despite this reduction, the high-resolution STEM images we acquired still retain distinguishable features, such as amorphous regions and graphene-like areas, enabling us to discern between high-oxidation and low-oxidation regions in the pristine GO sample.

2.3. The Structural Changes of GO Membranes after RO Filtration

GO membrane exhibits insufficient stability in RO experiments. **Figure 2a** illustrates the changes in GO nanochannels during pressure-driven filtration experiments. The expansion of interlayer spacing arises not only from the filling of nanochannels by water but also from damage to the 2D channels, particularly at the hydrophilic gate, which is the gap between the edges of two neighboring GO nanosheets or defects within the GO structure.[25] iDPC-STEM images (Figure 2b,c) reveal the formation of folding, distortion, and damage in monolayer and bilayer GO flakes derived from the filtration process, locally creating three-layered carbon atomic structures, which are discerned by the intensity in line profiles (Figure 2d). Such physical damage has compromised the GO membrane filtration capability. XRD spectrum (Figure 2e) also reveals interlayer spacing of wet GO membrane expands with filtration cycles. After removing the water from the GO channels, achieved by storing the membrane in a drying box at room temperature overnight, the XRD spectrum reveals that the interlayer spacing of the dry GO membrane increases from d = 0.769 nm before filtration to d' = 0.829 nm after RO filtration. This is primarily a result of the inherent folding and wrinkles of GO layers instead of the swelling issue, which is a common phenomenon in 2D materials from external force.[26] These structural changes in atomic scale reduce the salt rejection (Na^+) from $13.62 \pm 2.5\%$ (first cycle) to $3.6 \pm 1.6\%$ (second cycle) with a slight change in water permeance (from 5.62 ± 0.81 to 5.2 ± 1.34 L bar^{-1} h^{-1} m^{-2}), as shown in Figure 2f. Besides, in repeated filtration experiments on the same pristine GO membrane, the results show that as time increases, the pristine

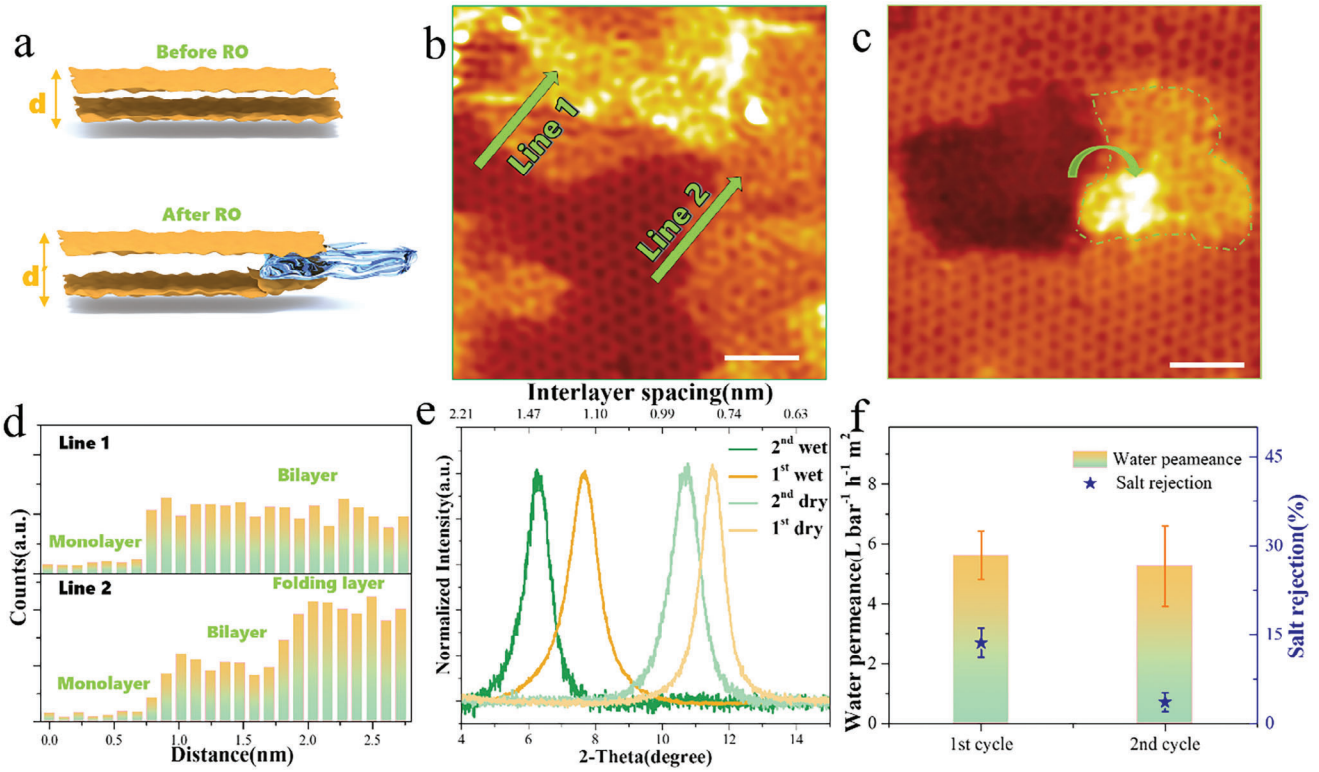

Figure 2. Structural deformation of GO under pressure-driven filtration a) Schematic illustration of structural changes of GO by salt water under external pressure. b) and c) iDPC-STEM images of folding and ripping of GO sheets after RO filtration. Scale bar 1 nm. d) Line profiles of intensity as a function of position showing layer thickness variation along the arrows in b). e) XRD measurement of GO membrane after two-cycle RO process. f) Water permeance and salt rejection of GO membrane of two-cycle RO process. Means (M) with error bars for three cases: N = 3, and the bars also show standard deviation (SD).

GO membrane gradually loses its screening effect on salt (Na^+) cations, as shown in Figure S11 (Supporting Information). This highlights the gradual impact of repeated usage in the RO filtration process on the structure of the GO membrane.

2.4. RO Filtration for GO Membranes via External Pressure

To further compare the impact of structural changes on GO filtration efficiency, we test the RO filtration performance of different GO membranes mainly composed of monolayer GO sheets with different sizes. The GO membranes are deposited on a commercial AAO substrate to measure the water and salt transport behaviors toward Na^+ solution at a concentration of 2000 parts per million (ppm). The GO membrane on AAO support demonstrates sufficient mechanical strength to sustain pressures at 2–40 bar. Different GO membranes which are composed of monolayer GO nanosheets with different sizes are made from various GO liquid dispersions. The GO dispersions are separated into three groups using high-speed centrifugation (refer to the methods section). Monolayer GO dispersions are selected based on the histogram of data distribution results and AFM topography analysis (**Figure 3a–c**). The GO membranes are named based on the particle size of the individual monolayer GO sheets. Different GO membranes are named GO_0.5, GO_1.0, and GO_2.0, respectively, where the number means the average size (unit: μm) of individual GO sheets. Besides, we also confirm that these samples have similar defect density and oxygen-containing functional groups by comparing the I_D/I_G and I_{2D}/I_G ratios as shown in Figure S12 and Table S3 (Supporting Information).

The GO membranes are sealed in a commercial dead-end filtration system with an effective membrane area of ≈7.5 cm^2 for the pure water permeation and salt rejection tests, as shown in Figure 3d. The results of the RO experiment are in Figure 3e, and we found with the increase of external pressure, a climb of salt rejection can be found while at the same time, the water permeance showed a decreasing trend. Certain investigations have indicated that increased feed pressure contributes to the improved salt rejection in GO membranes within the narrowed transport channels.[16c]

The channel spacing for wet GO membrane at different external pressure is measured by a reported method as shown in Figure S14 (Supporting Information). The interlayer spacing of the original GO film without external pressure in the wet state was measured from the XRD, while the interlayer spacing of the wet GO under pressure was calculated based on its total thickness, as described by Figure S14 (Supporting Information). Under external pressure 2–40 bar swelling of the wet GO membrane in the vertical direction is inhibited, resulting in a smaller channel (interlayer) spacing ranging from 0.85 (1.19) to 0.66 (1.00) nm, as shown in Figure 3f. Correspondingly, in our filtration experiments, we observed the highest salt rejection, reaching ≈25%

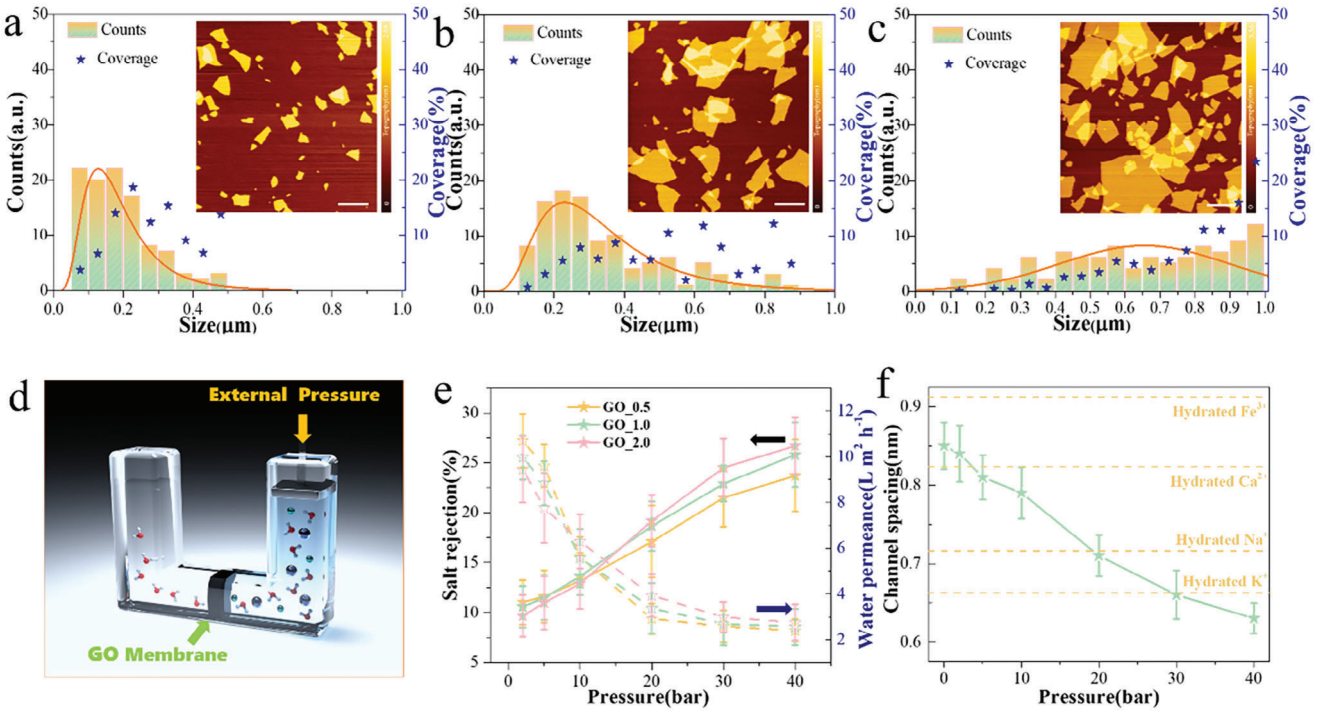

Figure 3. RO experiment of GO membrane with varying sizes of individual units at different external pressures. a–c) Histogram analysis of size and coverage distribution of different monolayer GO nanosheets with a particle size of a) 0.1-0.5 μm; b) 0.1-1 μm and c) 0.1-2 μm, respectively. Inset images are AFM topography images related to a), b), and c), respectively. Scale bar 1 μm. d) Schematic illustration of the dead-end RO system for the filtration experiment. e) Water permeance and salt rejection of GO membranes with different flake sizes (unit: μm) under different external pressures. f) Channel spacing of GO membrane under different external pressures. Means (M) with error bars for three cases: N = 3, and the bars also show standard deviation (SD).

at 40 bar when the channel spacing is ≈0.66 nm, which is less than most of the hydrated cations in our filtration experiment (Figure 3f). The relative lower salt rejection at this pressure is due to the mechanical deformation along the edges of GO layers, as we mentioned in the last section. As the feeding pressure increases, the water permeance increases, causing more severe mechanical deformation and damaging the slip path among the layers of the GO membrane, which is manifested in the increase in the interlayer spacing of the GO film in the dry state (Figure S15, Supporting Information). While the deformation will not keep increasing the interlayer spacing of GO in dry stage when the pressure is over 10 bar as we found that the expansion of the channel spacing in dry stage is similar at 10–40 bar. It shows that increased pressure also helps the GO membrane maintain its atomic structure when the pressure is over 10 bar.

It is important to note that GO membranes composed of monolayer GO of varying sizes exhibit distinct performance (Figure 3e). Specifically, at 2–5 bar, the GO_0.5 membrane demonstrates the highest salt (Na^+) rejection, while at 10–40 bar, GO_2.0 showed the best performance. TEM characterizations were conducted on the exfoliated monolayer GO samples after filtration, revealing that under low external pressure, edge deformation is considerably smaller compared to that at high pressure (Figure S16). Statistics in the Table S4 and Figure S17 (Supporting Information) show that at low pressure (2 bar), it is more conducive to capture ions at the holes and edges, while at high pressure (40 bar), the opposite trend is found. At 2 bar, a chain of some Na^+ ions was observed in the edge and pores of monolayer GO sheets, affirming their ability to adsorb and trap cations under weak feed pressure. However, the adsorption capacity of oxygen-containing functional groups was found to be suppressed at such pressure. In contrast, under high pressure, the interlayer spacing decreased, bringing the upper and lower GO sheets closer. A large number of Na^+ cations were found in the area with a high density of functional groups at 40 bar.

Due to the rapid water flux (Figure S18, Supporting Information) and edge deformation at 10–40 bar, the binding capacity for cations at edges and holes was reduced compared to that at 2–5 bar. In addition, the deformation of edges is limited in restricting the passage of Na^+ cations (Figure S19, Supporting Information). Consequently, the salt rejection of the GO membrane with a smaller monolayer unit (GO_0.5) was observed to be lower than that of the larger layer GO membrane at 10–40 bar, attributable to its numerous edge deformation. Therefore, increasing the external pressure reduces the interlayer spacing and simultaneously enhances the trapping of ions by functional groups in the intralayer of GO, but at the same time weakens the confinement effect of GO defects and edges on cations.

To further explore the ion-sieving capabilities of the GO membrane, we also tested the RO experiment with different salt solutions (K^+, Ca^{2+}, and Fe^{3+}), as shown in Figure S20 (Supporting Information). The trend behavior of K^+ ions with GO membrane is similar to that of Na^+ cations. High-valent cations are less affected by the channel spacing, and increasing the

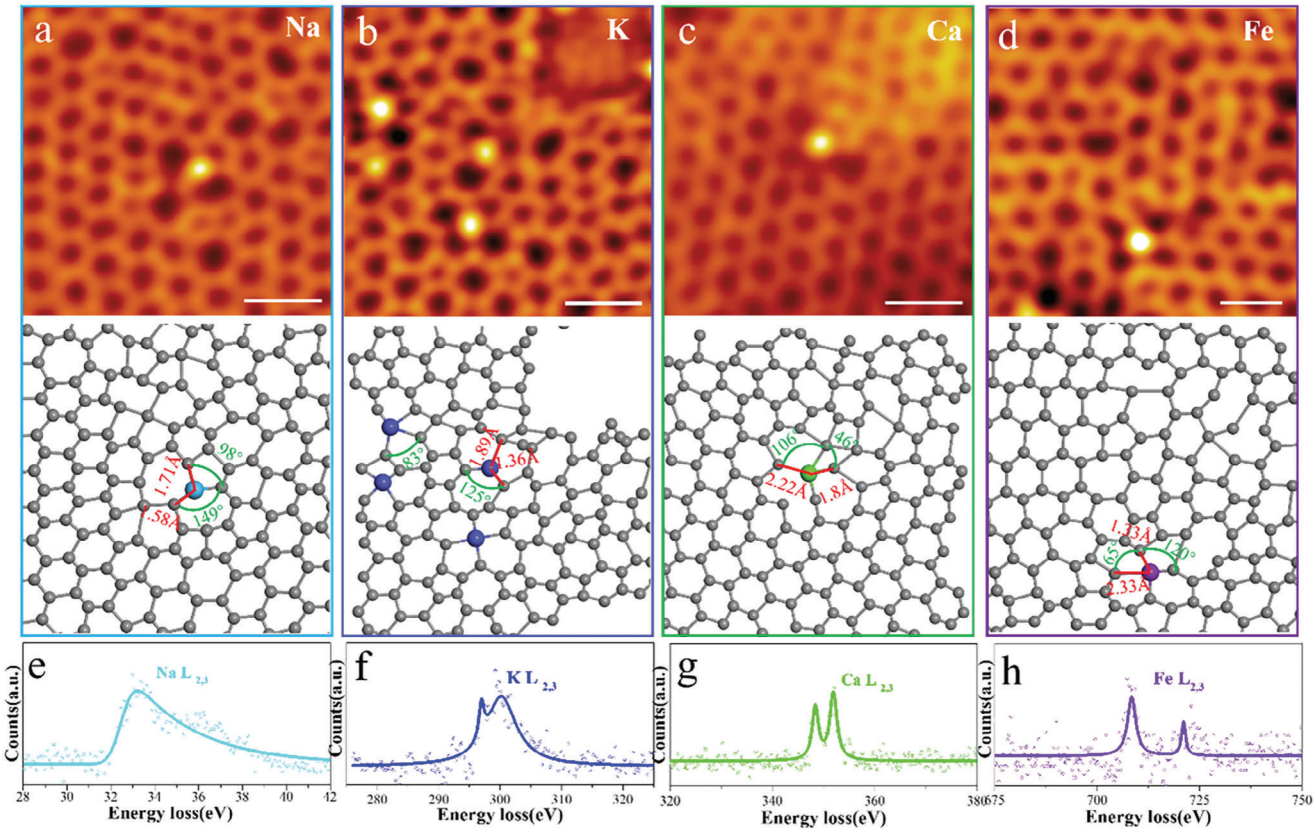

Figure 4. TEM characterization of metal ions on GO basal plane (Azure-Na, blue-K, cyan-Ca, and purple-Fe). High-resolution iDPC-STEM images of a) Na^+ b) K^+ c) Ca^{2+} d) Fe^{3+}ions on GO basal plane. Scale bar 500 pm. e–h) Atomic scale EEL spectra of Na, K, Ca, and Fe element on GO basal plane corresponding to a–d), respectively.

pressure does not significantly change their salt rejection. In particular, for Fe^{3+} ions, the ion selectivity of the GO membrane is not limited by swelling in water even at 2 bar, because of the relatively large hydrated radius and stronger interactions. Besides, for divalent cations (Ca^{2+}) and trivalent ions (Fe^{3+}) in this experiment, not only is the salt rejection much higher than those of monovalent ions, but it also exhibits a noticeable increase with GO membranes with larger monolayer units at all the external pressure used (Figure S19, Supporting Information). In addition, unlike monovalent cations, the GO_2.0 membrane always maintained the highest salt rejection to Ca^{2+} ions and Fe^{3+} ions, which is not related to the external pressure. The relatively strong interaction between divalent and trivalent ions and the functional groups, pores, and edges of the GO membrane makes the selectivity of the GO membrane much stronger than that of monovalent ions. It is surprising that for the GO_0.5 membrane composed of a smaller monolayer of GO sheets, the ion sieving capacity for Ca^{2+} and Fe^{3+} is always smaller than the GO_2.0 membrane. The three types of GO membranes differ only in the particle size of the monolayer GO samples they constitute, but the defect density and oxidation degree are the same (Figure S10 and Table S3, Supporting Information). XRD measurement also revealed that the performance is not related to the interlayer spacing (Figure S21, Supporting Information). The difference related to ion trapping is only reflected in the difference in the size of the three types of GO membranes. TEM analysis shows that, unlike monovalent ions, Ca^{2+} ions and Fe^{3+} ions will aggregate along the edges of GO to form clusters, which will destroy the structure of the edges (Figure S22, Supporting Information). Therefore, the GO_0.5 membrane with longer edges exhibits weaker ion selectivity than the GO_2.0 membrane. Our experiments show that the structural deformation of GO edges is one of the reasons that affect the filtration performance, making the edges of GO unable to capture ions in the RO process.

2.5. Atomic Structures of Trapped Cations on GO after RO Experiments

To gain a thorough understanding of the interplay between ions and GO membranes during RO filtration, we conducted STEM analysis on the post-filtration monolayer and few-layer GO nanosheets by mechanical exfoliation. Shown in **Figure** 4a–d, we find Na^+, K^+, Ca^{2+} and Fe^{3+}ions on the basal plane of monolayer GO, the element types for these absorbed atoms on GO are confirmed by EEL spectra results (Figure 4e,f). In these images, the ions are embedded in a disordered carbon lattice, which is different from the typical six-membered rings of graphene. The amorphous structure originates from the reduction of functional groups in GO, whereas the presence of impurity cations makes these structures more unstable during measurement. These ions are surrounded by 3–4 carbon atoms, with distances ranging

from 1.3 to 2.3 Å, and angles varying between 46° and 150° as shown in Figure 4. Besides, it shows the statistical results for single ions combined with GO plane in Table S5 (Supporting Information), showing the bond lengths and angles. However, for clusters containing more than one ion, it is challenging to provide comprehensive statistical analyses due to the numerous possible structural configurations. The complexity arises from the various arrangements and orientations of ions within the cluster, leading to a wide range of potential bond distances and angles. The cations are captured by charged groups from electrostatic interaction and other kinds of weak interaction, like cation-π bonding.[27] In contrast, the graphene-like regions have difficulty in adsorbing ions due to relatively weak interaction (Figure S23, Supporting Information). It matches the slip theory,[28] saline water flows quickly in the non-oxidation zone of the GO layers, while the oxygen-rich area hinders this rapid flow due to strong interactions so that the cations are easy to be captured. Furthermore, in comparison to monovalent ions, divalent and trivalent ions are more readily trapped by oxygen functional groups in the intralayer of GO by their stronger interactions. In our filtration experiments for the same concentration salt solutions, a few Na^+ and K^+ ions can be found in TEM images, while Ca^{2+} and Fe^{3+} ions exhibit higher adsorption properties and even formed ion clusters (Figures S24 and S25, Supporting Information). Conversely, monolayer GO with uniformly distributed single cation is observed when feeding different concentration salt solutions (Figure S26, Supporting Information).

For ultrathin membranes made up of monolayer GO nanosheets, the primary pathways for transporting substances are the edges of the GO nanosheets and the pores on their surfaces ranging from 0.5 to 3 nm (Figure S27, Supporting Information). These pathways are crucial for determining which particles can pass through the membrane and which ones are blocked.[29] In our STEM images, we observed pores of varying sizes distributed throughout the GO (Figure 2a). The edges of pores also can capture ions shown in Figures S28 and S29 (Supporting Information). The edges of pores lack a specific structure and do not appear as clean zigzag or armchair boundaries as graphene, with the majority of them being in an amorphous state. Although the diameter of some pores is much larger than that of the cations and their hydration radius, the adsorption at the edges is primarily guided by stronger π-π interactions near the edges of these pores, along with stronger hydrogen bonding interactions between carboxyl groups and cations.[30]

The adsorption of cations by the edges of macropores as observed suggests that ions can also be captured at the edges of the GO layer. In the case of Ca^{2+} and Fe^{3+} ions, the presence of ion clusters is noticed along the layer's edges. A substantial quantity of clusters is observed in the region where curling or deformation has taken place (Figure S22, Supporting Information). This phenomenon elucidates why the structure of the GO membrane is destroyed, especially the deformation along the edges (Figure 2), whereas the salt rejection of Ca^{2+} and Fe^{3+} ions remains relatively high (Figure S20, Supporting Information). These complex structures are more conducive to the adsorption of large amounts of ion clusters. Previous studies on nanofiltration using GO membranes have emphasized the control of subnanometer-sized pores, interlayer distribution, or the role of charge repulsion.[31] Our study demonstrates that the ion rejection reactions in the RO process are complex, confirming that they are driven by intricate interactions rather than a simple effect. High-resolution STEM images provide direct experimental evidence that the structures of GO, particularly the pore defects, functional groups, and ion-ion interactions, can all influence the filtration performance of GO membranes.

2.6. Cation-Absorbed GO Membranes

After RO filtration, there is a certain concentration of cations left in the channels of the GO membrane, and these ions interact with the GO layers to form a relatively stable structure following the filtration experiment. This interaction generates a high energy barrier, effectively discouraging the retention of cations in filtration.[32] To elucidate the mechanism of GO membranes based on ion repulsion, we introduced different types of cations (K^+, Ca^{2+}, and Fe^{3+}) to modify the pristine GO_2.0 membrane (see methods). We find that the Fe^{3+} coated GO_2.0 membrane (GO_Fe) shows the highest salt (Na^+) rejection rate up to 22.5 ± 2.76% at 10 bar, which is nearly two times higher than the pristine GO_2.0 membrane, as shown in **Figure 5**a. The ion selectivity exhibited by the GO_cation membrane is not related to the interlayer spacing, because GO_K^+ has the smallest interlayer spacing (Figure 5b) while it showed the lowest salt rejection compared to others. The GO_Fe membrane also exhibits durability and will not reduce the salt rejection rate multiple times, as evidenced in Figure 5c. Besides, we also find the performance of the GO_Fe membrane is related to the membrane thickness. With an increase of thickness from 100 to 400 nm, the salt rejection shows a climb up from ≈82% to ≈98% for Fe^{3+} and from 23% to ≈30% for Na^+, as shown in Figure S30 (Supporting Information).

Cations impact the GO membrane through non-covalent cation-π interactions with aromatic rings on GO sheets and interactions with oxygen-containing functional groups.[1b] Figure 4 and Figure S27 (Supporting Information) display that cations are trapped in the area with functional groups and defects. These cations remain stable during RO filtration and help to reject other cations getting into the GO channels (Figure 5d). These Fe^{3+} ions improve the performance of the membrane via electrostatic repulsion and cooperate with the adsorption of ions by the functional groups and defects are present in the GO membrane. After filtration with feeding with 2000 ppm NaCl solution, we still can find the presence of Fe^{3+} ions at the edge of the pores and inside the channels of adjacent GO layers (Figure 5e,f; Figure S31, Supporting Information). Besides, the EDS results in Figure 5g and Table S6 (Supporting Information) also reveal the atomic ratio changes of Fe^{3+} ions before and after the filtration experiment is less than 0.1%. It is proved that there are many more Fe^{3+} ions present in the GO_Fe membrane than those lost. To explore the changes in GO structure after filtration, Raman characterization was introduced, as shown in Figure 5h and Table S7 (Supporting Information). Compared to pristine GO without cation modification in Figure S10 (Supporting Information), the intensity of D peaks (I_D/I_G) shows an increase from 1.15 to 1.23, which is related to the increase of defects during RO filtration steps. There is more edge deformation and pores are generated during pressure-driven RO steps. The intensity of 2D peaks (I_{2D}/I_G) remains stable at 0.06, which demonstrates that there are no

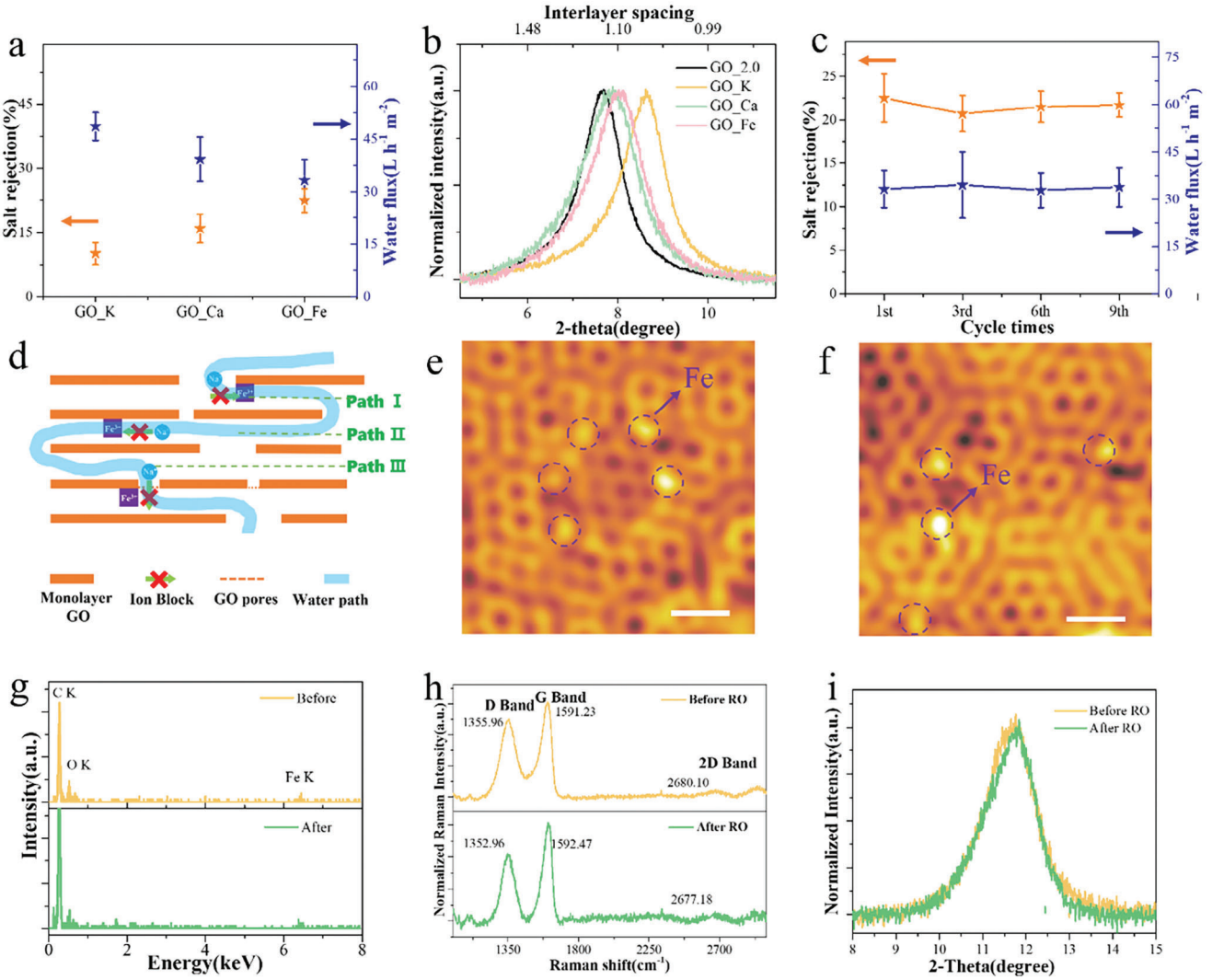

Figure 5. Filtration experiment of GO membrane via cation modification. a) Filtration performance of GO_cation membranes. b) XRD measurement of different GO_cation membranes in a wet state. c) Duration test of water flux and salt rejection of GO_Fe membrane. d) Schematic illustration of Na^+ ion blocked by Fe^{3+} at different regions in GO_Fe membrane. e) iDPC-STEM images of several Fe^{3+} ions trapped in edges of a bilayer GO after RO. Scale bar 500 pm. f) iDPC-STEM images of several Fe^{3+} ions trapped in interlayer channels (spacing) of a bilayer GO after RO. Scale bar 500 pm. g) EDS spectra of GO_Fe membrane before and after RO. h) Raman spectra of GO_Fe membrane before and after RO. i) XRD spectrum of GO_Fe membrane before and after RO at wet state. Means (M) with error bars for three cases: $N = 3$, and the bars also show standard deviation (SD).

changes in oxygen-containing during filtration. The FWHM of 2D peaks shows a climb from 84.35 to 90.95 cm^{-1}, which is caused by introducing doping Fe^{3+} cations when feeding $FeCl_3$ solution in RO. After filtration, the FWHW of the GO_Fe membrane shows a little drop from 90.95 to 88.46 cm^{-1} which is due to some of the doping Fe^{3+} ions being excluded by the water flux. While the intensity of the D and G peaks remains stable, it corresponds to the absence of any additional defects and oxygen-containing groups generated during filtration. Furthermore, as evidenced by the XRD result in Figure 5i, we also confirm that Fe^{3+} helps to inhibit swelling and the interlayer spacing shows no changes before and after filtration.

For the enhanced filtration performance, Na^+ or other cations are blocked by Fe^{3+} cations at 1) 2D interlayer channels (functional group), 2) surface defects (pores), and 3) hydrophilic gate, which are confirmed in the STEM images in Figure 5e,f and Figure S31 (Supporting Information). The stable Fe^{3+} adsorbed in this area via cation-π interaction helps to reject the cations to get into the GO channels. These Fe^{3+} ions are fixed at the above three positions and form a stable structure with the GO film under external pressure. Additionally, when considering that the dispersed single Fe^{3+} ions gradually agglomerate along the deformation of the GO edges under a pressure-driven filtration experiment, it is impossible to block the passage of Na^+ cations in some areas and hinders the capacity trade-off for ion and water sieving. In such cases, ion sieving primarily occurs within the lateral transmission process of the 2D channel and the longitudinal transmission through the defects (pores) in the GO_Fe membrane. It is worth noting that the selectivity of the GO_Fe membrane is also related to the number of Fe^{3+} ions in the channels,

and gradually becomes saturated as the Fe^{3+} ion concentration increases in the RO step, as shown in Figure S32 (Supporting Information). In this case, it does not mean that Fe^{3+} ions occupy all binding sites, while overall it is in an adsorption equilibrium state.[33] Most of the Fe^{3+} ions embedded in the GO lattice remain stable and will not be lost as the filtration proceeds. It must be emphasized that the ion screening mechanism here is mainly based on electrostatic repulsion.

Further experiments also demonstrate that a GO membrane with fewer exposed edges and larger monolayer GO sheets exhibits improved salt rejection (Figure S33, Supporting Information). This finding suggests that ion sieving is restricted at the edges of two adjacent GO layers. Additionally, we produced a mild-heating reduced GO_Fe (MrGO_Fe) film through a mild annealing process(see from method), which maintains a stable interlayer spacing to further resist swelling and obtain a higher salt rejection at ≈65%, as shown in Figures S34 and S35 (Supporting Information). It is proved that the seawater filtration performance of GO-based membrane can be further enhanced by introducing various interactions which include size effect, charge effect, and other weak interactions. This study provides valuable insights into process tuning and insertion of GO membranes, offering direct experimental evidence for the GO membrane filtration mechanism.

3. Conclusion

In summary, our study focuses on analyzing the ion-sieving mechanism of GO using advanced TEM techniques, specifically iDPC-STEM, in conjunction with RO filtration experiments of GO membranes. Through our investigation, we discovered the ion-capturing abilities of various components within GO channels. We found that functional groups of GO, edges between adjacent GO layers, and pores on the intralayer of monolayer GO sheets possess the capability to capture cations such as Na^+, K^+, Ca^{2+}, and Fe^{3+}. Notably, we emphasize the role of edges and defects (pores) in the GO film, which effectively block the passage of ions after swelling. Notably we observed that GO membranes via external pressure regulation or modified with high-valent cations demonstrate enhanced salt rejection performance compared to both the same and low-valent cations. This finding highlights the potential of cation modification in improving the filtration performance of GO membranes.The results provide valuable insights into process tuning, and ion sieving and insertion of GO membranes. We anticipate that our research will establish a solid groundwork for the advancement of cutting-edge filtration technologies.

4. Experimental Section

STEM Imaging: The STEM images were acquired using a state-of-the-art Spectra 300 microscope (FEI, USA), which features a double-Cs corrector, an acceleration voltage of 80 kV, and a low beam current of 10–20 pA to minimize sample damage. The atom-resolution images were recorded with 1024 × 1024 pixels for a field of view of 15–21.2 nm and dwell time of 10 µm per pixel using the annular dark field detector for HAADF-STEM images and segmented annular dark field detector for iDPC-STEM images. Each high-resolution atomic image was only exposed to beam irradiation when captured to avoid excessive beam damage and multiple scans. The convergence angle was set at 29.9 mrad, and the camera length is 145 cm, which resulted in a 40–200 mrad collection angle for HADDF and 9–38 mrad for iDPC-STEM. Post-acquisition processing techniques such as band-pass filtering and inverse fast Fourier transformation were employed to enhance image visibility and improve the quality of the images. EEL spectra were recorded using the Gatan Continuum K3, which comprises 1024 channels with a dispersion rate of 0.25 eV per channel, and the convergence angle is adjusted to 21.4 mrad with the smallest 29 cm camera length. The electron beam was focused on the angstrom level. Additionally, the single exposure time is 0.1s, and the total acquisition time is 1s to avoid beam damage. The EDS data are obtained using the Super-X detector with a data collection period of 30 s.

Raman Measurement: A Renishaw confocal Raman spectrometer was employed, equipped with a ×50 objective lens with ≈500 nm spot size. To enhance the Raman signal-to-noise ratio, the samples were transferred onto f-mica substrates before analysis. Raman scan is performed with two accumulations of 10 s.

Topographic Measurement: Topographic imaging was carried out using an AFM5300E system (Hitachi, Japan). To ensure minimal surface deformation during the topography observation, a Si-DF3-P2 cantilever (Hitachi, Japan) is employed, which had an estimated tip curvature of ≈10 nm. This cantilever was operated in tapping mode to acquire the topographic images.

Scanning Electron Microscope (SEM) Imaging: The cross-section of the GO membrane on the AAO membrane was visualized using an environmentally controlled Quattro ESEM (Thermo Scientific, USA) at 10 kV accelerated voltages. Before imaging, a thin layer of Au film was sputtered onto the sample surface to minimize the charging effect which can cause distortions in the resulting images. Although GO samples may generate fragments smaller than the size of AAO pore during ultrasonication process. As the vacuum filtration preparation progresses, the AAO pores gradually get filled with larger flakes of GO, which will prevent the smaller GO fragments from passing through the pores of the bottom GO channels. Instead, they gradually stack up, leading to an extension in the vacuum filtration preparation time.

Analysis of the Interlayer Spacing: X-ray diffraction (XRD) measurements were carried out using a SmartLab 9 kW – Advance diffractometer (Rigaku, USA) equipped with Cu Kα radiation (λ = 1.5406 Å). The measurements were conducted in the 2θ range of 5° to 30°, with a small step size of 0.02° and a fast-recording rate of 0.1 s. The interlayer spacing is calculated by Bragg's equation. It is expressed as Equation (1):

$$n\lambda = 2dsin\,(\theta) \tag{1}$$

where n is the order of diffraction, λ is the wavelength of the incident radiation, d is the spacing between the crystal planes, and θ is the angle between the incident radiation and the planes.

Preparation of GO Membrane: The GO membrane production cost is estimated ca. $5 per gram for a 0.628 m^2 GO membrane with 100 nm thickness. Aqueous suspension of GO was prepared by dispersing micrometer-sized GO flakes (purchased from Tanfeng Graphene Technology Co., Ltd., China) in distilled water using probe sonication for 1 h. GO dispersions containing different particle sizes were prepared by centrifugation. For instance, the preparation of the GO_0.5 membrane involved the centrifugation of a pristine GO dispersion in a high-speed centrifuge (10 000 rpm) for 10 min. Subsequently, the supernatant was carefully collected, and any remaining precipitation was removed. The collected precipitate was then measured to determine the total mass of the membrane. It was found that the GO membrane with a thickness of 100 nm requires 2 mg of GO materials. The centrifuge speed for GO_1.0 ranged from 5000 to 10 000 rpm and GO_2.0 is less than 5000 rpm. Next, a freestanding GO membrane was produced by vacuum filtering through a 47 mm diameter alumina membrane (Millipore, USA) filter with a pore size of 0.2 µm.

Preparation of GO_Cation Membrane: The cation-coated membrane was prepared by immersing the pristine GO_2.0 membrane into a 50 mL solution containing different types of salts at a concentration of 2000 ppm. Subsequently, an external pressure of 10 bar was applied for the reverse osmosis (RO) experiment until the water flux and salt rejection reached a

relatively stable state. Following the experiment, the surface salt solution was removed by rinsing the membrane three times with deionized water.

Preparation of rGO_Cation Membrane: The cation-coated reduced GO membrane was prepared by a reported method,[34] by putting the GO_Fe membrane into an oven for 24 h at 80 °C at air condition. A mild-heating reduced GO (MrGO) membrane was prepared by putting the GO membrane in the same condition.

RO Filtrations Experiments: Filtration tests were conducted using an HP4750X dead-end stirred cell (Sterlitech, USA), which was pressurized with Argon gas. Before RO, the membrane was sealed in the cell with ultrapure water at 5 bar overnight. The membranes were tested with deionized water or 2000 ppm of different salt solutions (NaCl, KCl, $CaCl_2$, and $FeCl_3$ were used here, Sigma-Aldrich, USA) at a constant pressure of 10 bar to determine their relative flux. The permeate flux (J) is calculated using Equation (2):

$$J = \frac{Q}{A \times T} \tag{2}$$

where Q represents the total permeate volume collected during the filtration time (*T*), while A denotes the effective cross-sectional area of the membrane in the filtration cell, measured in square meters (m^2). Magnetic stirring was employed to prevent concentration polarization effects. High-accuracy determination of the concentrations of ions, which diffuse through the membranes and enter the permeate compartment, is carried out using ion chromatography (IC) techniques and ion meter.

Statistical Analysis: In this study, all filtration experiments were performed in triplicate for each sample and analyzed with three technical replicates. The data is presented as mean values ± standard deviation. All the TEM images were filtered with bandpass filter to reduce noise. The statistical data on TEM images were obtained from no less than 50 images. All linear maps were created using Originlab software, and the STEM image spacing was measured using GMS 3 software.

Supporting Information

Supporting Information is available from the Wiley Online Library or from the author.

Acknowledgements

This work was supported by Shenzhen Science, Technology and Innovation Commission (project nos. JCYJ20200109110213442), National Science Foundation of China (project nos. 52222218, 52272045, 52173230), The Hong Kong Research Grant Council General Research Fund 2841 (project nos. 11312022, 15302522, 11300820), The Environment and Conservation Fund (project nos. 69/2021, 34/2022), City University of Hong Kong (project nos. 7006005, 9680241, 9678303), The State Key Laboratory of Marine Pollution (SKLMP) Seed Collaborative Research Fund SKLMP/SCRF/0037, The Hong Kong Polytechnic University (project nos. ZVH0 and SAC9), The Research Institute for Advanced Manufacturing of The Hong Kong Polytechnic University.

Conflict of Interest

The authors declare no conflict of interest.

Data Availability Statement

The data that support the findings of this study are available from the corresponding author upon reasonable request.

Keywords

atomic structure, defects, graphene oxide, iDPC-STEM, ion sieving

Received: March 6, 2024
Revised: June 12, 2024
Published online: June 28, 2024

[1] a) J. Abraham, K. S. Vasu, C. D. Williams, K. Gopinadhan, Y. Su, C. T. Cherian, J. Dix, E. Prestat, S. J. Haigh, I. V. Grigorieva, P. Carbone, A. K. Geim, R. R. Nair, *Nat. Nanotechnol.* **2017**, *12*, 546; b) L. Chen, G. Shi, J. Shen, B. Peng, B. Zhang, Y. Wang, F. Bian, J. Wang, D. Li, Z. Qian, G. Xu, G. Liu, J. Zeng, L. Zhang, Y. Yang, G. Zhou, M. Wu, W. Jin, J. Li, H. Fang, *Nature* **2017**, *550*, 380; c) S. Guo, S. Garaj, A. Bianco, C. Ménard-Moyon, *Nat. Rev. Phys.* **2022**, *4*, 247; d) R. K. Joshi, P. Carbone, F. C. Wang, V. G. Kravets, Y. Su, I. V. Grigorieva, H. A. Wu, A. K. Geim, R. R. Nair, *Science* **2014**, *343*, 752; e) R. R. Nair, H. A. Wu, P. N. Jayaram, I. V. Grigorieva, A. K. Geim, *Science* **2012**, *335*, 442; f) J. Shen, G. Liu, Y. Han, W. Jin, *Nat. Rev. Mater.* **2021**, *6*, 294.
[2] A. V. Talyzin, *Nat. Nanotechnol.* **2022**, *17*, 131.
[3] a) G. M. Geise, *Science* **2021**, *371*, 31; b) T. E. Culp, B. Khara, K. P. Brickey, M. Geitner, T. J. Zimudzi, J. D. Wilbur, S. D. Jons, A. Roy, M. Paul, B. Ganapathysubramanian, A. L. Zydney, M. Kumar, E. D. Gomez, *Science* **2021**, *371*, 72; c) Z. Tan, S. Chen, X. Peng, L. Zhang, C. Gao, *Science* **2018**, *360*, 518.
[4] a) Z. Jiang, S. Karan, A. G. Livingston, *Adv. Mater.* **2018**, *30*, 1705973; b) D. L. Shaffer, K. E. Feldman, E. P. Chan, G. R. Stafford, C. M. Stafford, *J. Memb. Sci.* **2019**, *583*; c) V. Freger, *Adv. Colloid. Interface. Sci.* **2020**, *277*, 102107.
[5] a) M. Fathizadeh, W. L. Xu, F. Zhou, Y. Yoon, M. Yu, *Adv. Mater. Interfaces* **2017**, *4*, 1600918. b) D. Chen, H. Feng, J. Li, *Chem. Rev.* **2012**, *112*, 6027.
[6] a) A. K. Geim, K. S. Novoselov, *Nat. Mater.* **2007**, *6*, 183; b) K. S. Novoselov, A. K. Geim, S. V. Morozov, D. Jiang, Y. Zhang, S. V. Dubonos, I. V. Grigorieva, A. A. Firsov, *Science* **2004**, *306*, 666.
[7] W. S. Hummers, Jr., R. E. Offeman, *JACS* **1958**, *80*, 1339.
[8] P. P. Brisebois, M. Siaj, *J. of Mater. Chem. C* **2020**, *8*, 1517.
[9] T. H. Ge, Z. Gao, J. Li, X. Zhan, *Membranes* **2023**, *13*, 220.
[10] a) P. Sun, F. Zheng, M. Zhu, Z. Song, K. Wang, M. Zhong, D. Wu, R. B. Little, Z. Xu, H. Zhu, *ACS Nano* **2014**, *8*, 850; b) J. Liu, G. Shi, P. Guo, J. Yang, H. Fang, *Phys. Rev.Lett.* **2015**, *115*, 164502.
[11] Y. Xue, H. Chen, D. Yu, S. Wang, M. Yardeni, Q. Dai, M. Guo, Y. Liu, F. Lu, J. Qu, L. Dai, *Chem. Commun.* **2011**, *47*, 11689.
[12] S. Zheng, Q. Tu, J. J. Urban, S. Li, B. Mi, *ACS Nano* **2017**, *11*, 6440.
[13] a) J. Wei, Y. Hu, Y. Liang, B. Kong, Z. Zheng, J. Zhang, S. P. Jiang, Y. Zhao, H. Wang, *J. Mater. Chem. A* **2017**, *5*, 10182; b) W. H. Zhang, M. J. Yin, Q. Zhao, C. G. Jin, N. Wang, S. Ji, C. L. Ritt, M. Elimelech, Q. F. An, *Nat. Nanotechnol.* **2021**, *16*, 337.
[14] W. Zhang, H. Xu, F. Xie, X. Ma, B. Niu, M. Chen, H. Zhang, Y. Zhang, D. Long, *Nat. Commun.* **2022**, *13*, 471.
[15] X. Chen, W. Wang, L. Zhu, C. Liu, F. Cui, N. Li, B. Zhang, *ACS Appl. Nano Mater.* **2021**, *4*, 673.
[16] a) M. Zhang, K. Guan, Y. Ji, G. Liu, W. Jin, N. Xu, *Nat. Commun.* **2019**, *10*, 1253; b) W. J. Paschoalino, N. A. Payne, T. M. Pessanha, S. M. Gateman, L. T. Kubota, J. Mauzeroll, *Anal. Chem* **2020**, *92*, 10300. c) W. Li, W. Wu, Z. Li, *ACS Nano* **2018**, *12*, 9309.
[17] A. Boretti, S. Al-Zubaidy, M. Vaclavikova, M. Al-Abri, S. Castelletto, S. Mikhalovsky, *npj Clean Water* **2018**, *1*, 5.
[18] D. C. Marcano, D. V. Kosynkin, J. M. Berlin, A. Sinitskii, Z. Sun, A. Slesarev, L. B. Alemany, W. Lu, J. M. Tour, *ACS Nano* **2010**, *4*, 4806.
[19] a) O. Kwon, Y. Choi, E. Choi, M. Kim, Y. C. Woo, D. W. Kim, *Nanomaterials* **2021**, *11*, 757; b) E. Yang, C. M. Kim, J.-h. Song, H. Ki, M. H. Ham, I. S. Kim, *Carbon* **2017**, *117*, 293.
[20] a) E. Yücelen, I. Lazić, E. G. T. Bosch, *Sci. Rep.* **2018**, *8*, 2676; b) I. Lazić, E. G. T. Bosch, S. Lazar, *Ultramicroscopy* **2016**, *160*, 265.

[21] C. Hofer, V. Skákalová, T. Görlich, M. Tripathi, A. Mittelberger, C. Mangler, M. R. A. Monazam, T. Susi, J. Kotakoski, J. C. Meyer, *Nat. Commun.* **2019**, *10*, 4570.
[22] C. T. Toh, H. Zhang, J. Lin, A. S. Mayorov, Y. P. Wang, C. M. Orofeo, D. B. Ferry, H. Andersen, N. Kakenov, Z. Guo, I. H. Abidi, H. Sims, K. Suenaga, S. T. Pantelides, B. Özyilmaz, *Nature* **2020**, *577*, 199.
[23] K. N. Kudin, B. Ozbas, H. C. Schniepp, R. K. Prud'homme, I. A. Aksay, R. Car, *Nano Lett.* **2008**, *8*, 36.
[24] a) A. Radoń, P. Włodarczyk, D. Łukowiec, *Physica E* **2018**, *99*, 82; b) A. Y. S. Eng, C. K. Chua, M. Pumera, *Nanoscale* **2015**, *7*, 20256.
[25] J. Wang, P. Zhang, B. Liang, Y. Liu, T. Xu, L. Wang, B. Cao, K. Pan, *ACS Appl. Mater. Interfaces* **2016**, *8*, 6211.
[26] Y. Zhang, S. Zhang, J. Gao, T. S. Chung, *J. Membr. Sci.* **2016**, *515*, 230.
[27] L. Mu, Y. Yang, J. Liu, W. Du, J. Chen, G. Shi, H. Fang, *Phys. Chem. Chem. Phys.* **2021**, *23*, 14662.
[28] H. Tang, Y. Zhao, S. Shan, X. Yang, D. Liu, F. Cui, B. Xing, *Environ. Sci. Technol.* **2018**, *52*, 7689.
[29] X. Wen, T. Foller, X. Jin, T. Musso, P. Kumar, R. Joshi, *Nat. Commun.* **2022**, *13*, 5690.
[30] R. He, S. Cong, J. Wang, J. Liu, Y. Zhang, *ACS Appl. Mater. Interfaces* **2019**, *11*, 4338.
[31] a) J. S. Jang, J. Lee, W. T. Koo, D. H. Kim, H. J. Cho, H. Shin, I. D. Kim, *Anal. Chem.* **2020**, *92*, 957; b) S. Pang, D. Peng, Y. Hao, B. Song, X. Zhang, L. Jiang, *Matter* **2023**, *6*, 1173.
[32] Y. G. Yan, W. S. Wang, W. Li, K. P. Loh, J. Zhang, *Nanoscale* **2017**, *9*, 18951.
[33] W. Konicki1, M. Aleksandrzak, E. Mijowska, *Pol. J. Chem. Technol.* **2017**, *19*, 120.
[34] S. Y. Li, Y. Xia, W. Zhao, C. D. Easton, C. Selomulya, X. Zhang, *J. Memb. Sci.* **2020**, *601*, 117900.
[35] A. G. Volkov, S. Paula, D. W. Deamer, *Bioelectrochem. Bioenerg.* **1997**, *42*, 153.
[36] S. Yuan, Y. Li, Y. Xia, C. Selomulya, X. Zhang, *J. Memb. Sci.* **2021**, *621*, 118995.
[37] K. Guan, Y. Guo, Z. Li, Y. Jia, Q. Shen, K. Nakagawa, T. Yoshioka, G. Liu, W. Jin, H. Matsuyama, *Nat. Commun.* **2023**, *14*, 1016.
[38] K. Guan, Y. Jia, Y. Lin, S. Wang, H. Matsuyama, *Nano Lett.* **2021**, *21*, 3495.
[39] A. Morelos-Gomez, R. Cruz-Silva, H. Muramatsu, J. Ortiz-Medina, T. Araki, T. Fukuyo, S. Tejima, K. Takeuchi, T. Hayashi, M. Terrones, M. Endo, *Nat. Nanotechnol.* **2017**, *12*, 1083.
[40] Y. Wu, C. F. Fu, Q. Huang, P. Zhang, P. Cui, J. Ran, J. Yang, T. Xu, *ACS Nano* **2021**, *15*, 7586.

